Journal of Materials Chemistry A

ROYAL SOCIETY OF CHEMISTRY

PAPER

View Article Online
View Journal | View Issue

Cite this: *J. Mater. Chem. A*, 2023, **11**, 14015

Low-temperature pyrolysis enables $FeNi_3$ nanoparticle implanted N-doped carbon nanosheets as an efficient bifunctional electrocatalyst for overall water splitting†

Rong Xin,[a] Yijiang Liu, *[a] Xuxin Li,[a] Shicheng Yi,[a] Mingyue Zhang, [b] Hongbiao Chen,[a] Huaming Li[a] and Zhiqun Lin *[b]

The creation of highly efficient and stable OER/HER bifunctional electrocatalysts is vital to advancing the practical application of electrocatalytic water splitting. Herein, we propose a facile yet reliable approach to produce $FeNi_3$ nanoparticle (NP) implanted N-doped carbon nanosheets (denoted as $FeNi_3$/NCS) as a powerful bifunctional catalyst towards electrocatalytic water splitting. Specifically, a melamine tube is first synthesized *via* a hydrothermal method, which is utilized as a self-supporting template to grow FeNi-LDH, yielding melamine tube@FeNi-LDH. Sequentially, the $FeNi_3$ NP embedded N-doped carbon nanosheets are achieved by low-temperature pyrolysis of melamine tube@FeNi-LDH at 400 °C. The resulting $FeNi_3$/NCS electrocatalyst displays outstanding OER/HER catalytic performance and stability in alkaline media. The overpotential for the OER is 260 mV, outperforming the control samples of NCT, FeNiO/C, FeNi/NC and even benchmark RuO_2 (300 mV). The HER overpotential is also significantly reduced compared with the control samples. The impressive bifunctional activity of $FeNi_3$/NCS is primarily attributed to the synergistic effect between $FeNi_3$ NPs and N-doped carbon, which is substantiated by both experimental results (*i.e.*, overpotential and XPS) and DFT simulation (*i.e.*, Gibbs free energy, electron density difference, *etc.*). The $FeNi_3$/NCS-assembled water splitting device requires only 1.53 V of cell voltage to drive a current density of 10 mA cm^{-2}, surpassing the counterparts of RuO_2–Pt/C, NCT, FeNiO/C, and various reported FeNi-containing electrocatalysts. The combination of hydrothermal and low-temperature pyrolysis strategies will shed light on the design and preparation of LDH-derived high-performance and stable bifunctional electrocatalysts for overall water splitting.

Received 27th March 2023
Accepted 25th May 2023

DOI: 10.1039/d3ta01819a

rsc.li/materials-a

[a]*College of Chemistry and Key Laboratory of Environmentally Friendly Chemistry and Application of Ministry of Education, Xiangtan University, Xiangtan 411105, Hunan Province, China. E-mail: liuyijiang84@xtu.edu.cn; z.lin@nus.edu.sg*

[b]*Department of Chemical and Biomolecular Engineering, National University of Singapore, Singapore, 117585*

† Electronic supplementary information (ESI) available. See DOI: https://doi.org/10.1039/d3ta01819a

Dr Yijiang Liu is now a professor in the College of Chemistry at Xiangtan University, China. She received her M.S. degree from Xiangtan University in 2009 and PhD from the Institute of Chemistry, Chinese Academy of Sciences in 2015. She was a visiting scholar at the Georgia Institute of Technology during 2017–2018. Her research work focuses on the design and preparation of advanced functional materials: porous carbon materials for efficient and durable electrocatalysts in energy conversion and storage devices; the crafting of highly stable perovskite nanocrystals by using functional polymers as nano-reactors; Janus materials for concurrent catalysis and emulsification.

1. Introduction

The widespread exploration of clean and sustainable green energy sources is of great significance to mitigate the growing energy crisis and environmental pollution. Hydrogen, as one of the clean and sustainable green energy sources, has garnered extensive research attention owing to its high weight energy density and zero carbon emission.[1–3] Electrocatalytic water splitting for hydrogen generation is a promising technology for renewable clean energy.[4,5] There are two half-reactions in electrocatalytic water splitting, the oxygen evolution reaction (OER) in the anode and the hydrogen evolution reaction (HER) in the cathode.[6–8] However, the large overpotential and sluggish kinetics for the OER and HER have severely hindered the commercial application of electrocatalytic water splitting.[9–11] Noble metal-based electrocatalysts, such as Pt/C, and IrO_2/RuO_2, are considered the most active HER and OER electrocatalysts for water splitting, respectively.[12–15] Nonetheless, their insufficient reserves, high cost, and limited stability are unavoidable problems for large-scale utilization. Although noticeable advances have been achieved in the development of HER or OER electrocatalysts, the development of high-performance HER/OER bifunctional electrocatalysts still remains a grand challenge due to the incompatibility (*i.e.*, stability, activity) of HER and OER electrocatalysts in the same electrolyte.[16,17] Therefore, the rational design and facile fabrication of low-cost and highly active HER/OER bifunctional electrocatalysts for overall water splitting are extremely desirable.

In the past few years, great endeavours have been devoted to developing transition metal-based materials, such as carbides,[18–20] nitrides,[21,22] sulfides,[23–25] phosphide[26–28] metal oxides or hydroxides,[29–32] *etc.*, as efficient and stable electrocatalysts towards water splitting in alkaline electrolytes. Among them, transition metal-based layered double hydroxides (LDHs) consisting of divalent and trivalent transition metal cations and hydroxide ions have emerged as promising water-splitting electrocatalysts owing to their unique 2D layered architecture, tunable composition and earth-abundant sources.[33–35] FeNi-LDH has been verified to be a competitive alternative for the OER, but the HER performance is unfavorable, which is primarily caused by the intrinsic low conductivity and deficient electrochemically active surface area.[36] Doping with other metal nanoparticles,[37,38] coupling with conductive supports,[39–41] and hybridizing with other functional compounds[42–44] are effective ways to boost the electrocatalytic activity of LDHs. For instance, Ma and coworkers have reported NiFe LDH modified Ag nanowires on Ni foam to improve the OER and HER activity.[45] By coupling MOFs with LDHs, Zhai's group obtained the hetero-nanotree array catalyst of CoNiRu-NT, which integrated the Ru metal sites, conductive Ni foam and the hetero-interface between the MOF and the LDH, thereby affording low HER and OER overpotentials.[46] Recently, the Ir/Ni_3Fe/rGO catalyst was obtained by decorating Ir nanodots and FeNi-LDH on reduced graphene oxide followed by calcination, which exhibited superior OER performance to the benchmark IrO_2 and comparable HER activity to Pt/C.[47] The assembled electrolyzer using Ir/Ni_3Fe/rGO as the anode and cathode in alkaline solution delivered a cell voltage of 1.57 V at 10 mA cm^{-2}, largely surpassing the control samples. Significant progress has been made in boosting the electrocatalytic activity of transition metal-based LDHs; however, the LDH-derived transition metal implanted carbon materials by low-temperature pyrolysis with high OER/HER bifunctional activity and durability are relatively few and limited in scope.

Herein, we report a simple and robust strategy for crafting $FeNi_3$ nanoparticle (NP) implanted N-doped carbon nanosheets by low-temperature pyrolysis of the melamine tube@FeNi-LDH (Mel-T@FeNi-LDH) heterostructure as a highly efficient OER/HER electrocatalyst for overall water splitting. First, the melamine tube (Mel-T) was prepared by a hydrothermal method, which was utilized as a self-supporting template to *in situ* grow FeNi-LDH. Subsequently, $FeNi_3$ NP implanted N-doped carbon nanosheets (denoted as $FeNi_3$/NCS) were obtained after pyrolysis of Mel-T@FeNi-LDH at 400 °C for 2 h. The resulting $FeNi_3$/NCS exhibited remarkable OER and HER electrocatalytic activity with low overpotentials and excellent stability. The underlying mechanism for the obviously promoted OER/HER activity was assigned to the synergistic effect between $FeNi_3$ NPs and N-doped carbon nanosheets (NCS) as revealed by experimental results and DFT calculations. The high impact of the pyrolysis temperature on the electrocatalytic performance was also discussed. The assembled two-electrode electrolyzer using $FeNi_3$/NCS as the anode and cathode catalyst in 1.0 M KOH solution demonstrated a small cell voltage of 1.53 V at 10 mA cm^{-2} and excellent electrode stability, which is superior to the benchmark RuO_2–Pt/C, and the references of NCT, FeNiO/C counterparts.

2. Experimental section

2.1 Synthesis of the melamine tube (Mel-T)

Melamine (1.0 g) was added to 60 mL of deionized water at 90 °C under vigorous stirring and then transferred into a Teflon-lined stainless-steel autoclave. After the hydrothermal reaction at 180 °C for 24 h, the melamine tube was collected by centrifugation, followed by washing with deionized water several times and drying at 40 °C in a vacuum oven.

2.2 Synthesis of melamine tube@FeNi-LDH (Mel-T@FeNi-LDH)

50 mg of $Fe(NO_3)_3 \cdot 9H_2O$, 150 mg of urea, and 150 mg of $Ni(NO_3)_2 \cdot 6H_2O$ were entirely dissolved in 50 mL of deionized water under vigorous stirring. 100 mg Mel-T was then added and continuously stirred for 1.5 h at room temperature. Subsequently, the mixture was poured into a Teflon-lined stainless-steel autoclave and kept at 120 °C for 10 h. Finally, the collected solid product (denoted as Mel-T@FeNi-LDH) was washed with deionized water and ethanol several times and dried at 40 °C overnight.

2.3 Synthesis of $FeNi_3$/NCS

The obtained Mel-T@FeNi-LDH was placed into a porcelain boat and calcined at 400 °C (350 °C, 450 °C) for 2 h with

a heating rate of 5 °C min^{-1} under a nitrogen atmosphere. For comparison, the melamine tube, FeNi-LDH and the physical mixture of melamine tube and FeNi-LDH were pyrolyzed under identical conditions. The corresponding reference samples were labelled as NCT (pyrolyzed from the melamine tube), FeNiO/C (pyrolyzed from FeNi-LDH) and FeNi/NC (pyrolyzed from a mixture of melamine tube and FeNi-LDH).

3. Results and discussion

3.1 Synthesis and characterization of the $FeNi_3$/NCS electrocatalyst

The synthetic strategy of $FeNi_3$/NCS is schematically illustrated in Scheme 1. Melamine tubes (Mel-T) were first synthesized *via* a hydrothermal method at 180 °C, and FeNi-LDH nanosheets were further grown on the Mel-T *via* coordination and surface nucleation. The $FeNi_3$/NCS was finally obtained by low-temperature pyrolysis at 400 °C for 2 h. For comparison, the reference samples of NCT (pyrolyzed from the melamine tube without FeNi-LDH), FeNiO/C (pyrolyzed from FeNi-LDH without the melamine tube), and FeNi/NC (pyrolyzed from a mixture of melamine tube and FeNi-LDH) were obtained under identical pyrolysis conditions.

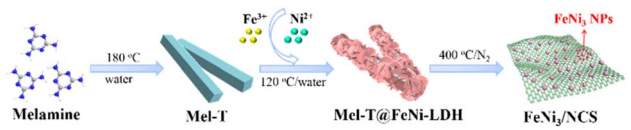

Scheme 1 Schematic illustration of the preparation of the $FeNi_3$/NCS electrocatalyst.

As shown in Fig. S1,† the solid melamine tube (Mel-T) was converted into nanosheets after pyrolysis at 400 °C. The sheet-like morphology of FeNi-LDH was well retained after pyrolysis under the same conditions and obvious metal oxide nanoparticles emerged (Fig. S2 and S6†). With the melamine tube as a self-supporting template, FeNi-LDH nanosheets were grown on the surface of the melamine tube, yielding the hetero-structured melamine tube@FeNi-LDH (Mel-T@FeNi-LDH) (Fig. 1a). The successful preparation of Mel-T@FeNi-LDH was verified by FTIR as shown in Fig. S3,† where the characteristic bands of –OH (1383 cm^{-1} and 3447 cm^{-1}) in FeNi-LDH and melamine (–C=N, –NH, and C–N) emerged in Mel-T@FeNi-LDH.[47,48] The variations of characteristic triazinyl (C=N) indicate the interaction between FeNi-LDH and $–NH_2$ groups of melamine. After pyrolysis at 400 °C, Mel-T@FeNi-LDH was transformed into $FeNi_3$ nanoparticle (NP) implanted N-doped carbon nanosheets ($FeNi_3$/NCS), as shown in Fig. 1b and c. The FeNi-LDH started to decompose at 300 °C (ref. 49) and gradually converted into $FeNi_3$ NPs at 400 °C accompanied by the transformation of the melamine tube into N-doped carbon nanosheets. The average diameter of $FeNi_3$ NPs is approximately 15 nm (Fig. 1d). The lattice spacing of 0.203 nm is assigned to the (111) plane of $FeNi_3$ NPs (Fig. 1e and Fig. S4†).[50,51] The X-ray

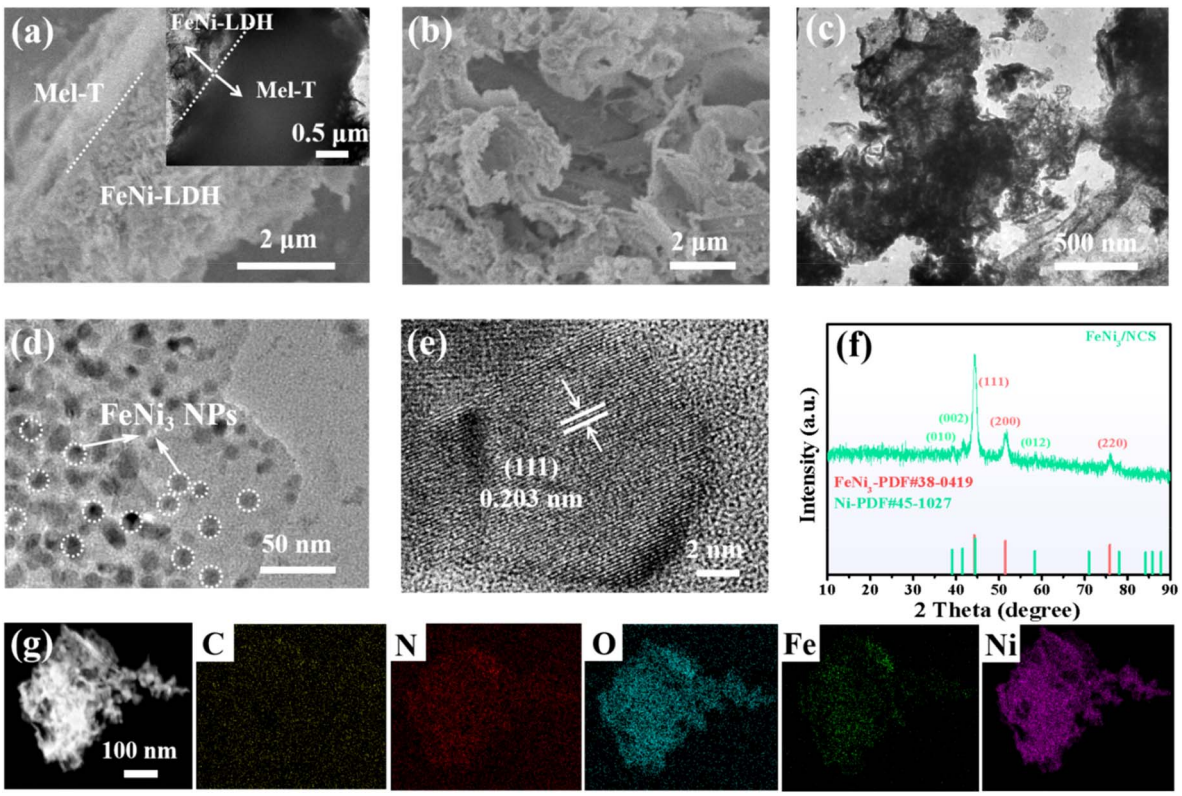

Fig. 1 SEM and inset TEM images of (a) Mel-T@FeNi-LDH; (b) SEM, (c and d) TEM, (e) HRTEM images, (f) XRD pattern and (g) elemental mapping images of $FeNi_3$/NCS.

diffraction (XRD) pattern of $FeNi_3$/NCS is depicted in Fig. 1f. The characteristic peaks at $2\theta = 44.28°$, 51.53°, and 75.86° can be indexed to the (111), (200), and (220) lattice planes of $FeNi_3$ (PDF#38-0419).[47,52] In addition, a small amount of Ni is indicated by the weak peaks appearing at 39.10° (010), 41.53° (002), and 58.42° (012) (PDF#45-1027). The control sample of FeNi/NC obtained by pyrolysis of the mixture of Mel-T and FeNi-LDH retains the sheet-like morphology but with large and aggregated nanoparticles as shown in Fig. S5.† The XRD patterns of the control samples are shown in Fig. S6.† The 2θ around 27.2° can be assigned to the C_3N_4 after pyrolysis of Mel-T. The XRD patterns of FeNi/NC are similar to those of $FeNi_3$/NCS, including $FeNi_3$ and a small amount of Ni, while obvious metal oxide peaks (*i.e.*, NiO, Fe_3O_4) are observed in FeNiO/C. Elemental mapping images in Fig. 1g demonstrate the homogeneous distribution of C, N, O, Fe and Ni. The surface oxidation of $FeNi_3$ NPs, when exposed to air, may be responsible for the emerging O element. It is noteworthy that the optimal ratio of Mel-T : $Fe(NO_3)_3 \cdot 9H_2O$: $Ni(NO_3)_2 \cdot 6H_2O$ was set to 2 : 1 : 3 after scrutinizing the OER and HER activities of the as-prepared samples with various ratios (Fig. S7†). The detailed characterization and electrocatalytic activity were primarily concentrated on $FeNi_3$/NCS with the optimized composition in the following content.

X-ray photoelectron spectroscopy (XPS) was performed to elucidate the chemical composition and element valence of the $FeNi_3$/NCS electrocatalyst. As plotted in Fig. 2a, the full survey spectrum indicates the presence of C, O, N, Fe, and Ni elements. In the high-resolution Fe 2p spectrum (Fig. 2b), the two peaks at 707.29 and 720.60 eV are assigned to $2p_{3/2}$ and $2p_{1/2}$ of Fe^0, while the peaks centered at 709.45/722.68 eV and 711.25/724.74 eV belong to Fe^{2+} and Fe^{3+}, respectively.[52,53] Similarly, the high-resolution Ni 2p can be deconvoluted into Ni^0 (852.81 and 869.72 eV), Ni^{2+} (854.36 and 872.60 eV), Ni^{3+} (856.03 and 874.15 eV) and satellite peaks (861.4 eV and 879.42 eV) (Fig. 2c).[54] The existence of Fe^0 and Ni^0 signifies the metallic Fe and Ni in $FeNi_3$ alloyed NPs. The deconvoluted N 1s XPS spectrum indicates the presence of two N-species, *i.e.*, pyrrolic N, and pyridinic-N at the binding energies of 399.95 eV and 398.80 eV (Fig. 2d).[55] The pyridinic-N can regulate the electronic structure of adjacent carbon atoms, thus improving the OER activity. The high-resolution C 1s spectrum is deconvoluted into C–C, C–N and C=O at 284.81 eV, 286.55 eV, and 288.20 eV, respectively (Fig. 2e).[56] In the high-resolution O 1s spectrum, the peaks located at 530.70 eV, 531.78 eV, and 533.10 eV can be assigned to metal–O (M–O), hydroxyl group oxygen (*i.e.*, M–OH) and absorbed water (H_2O), respectively (Fig. 2f).[52] Notably, the M–O may originate from the surface oxidation of the alloyed NPs. The Raman spectrum of the $FeNi_3$/NCS electrocatalyst was further measured to investigate graphitization. As shown in Fig. S8,† there are two obvious peaks at around 1366 cm^{-1} and 1601 cm^{-1}, corresponding to the D band and G band of $FeNi_3$/NCS. The I_D/I_G ratio of 1.03 suggests more structure defects of the carbon, benefiting the exposure of active sites.[39,57] The emerging band located between 500 and 700 cm^{-1} is related to the M–O bond, in line with the XPS analysis.[39] In addition, the specific surface area and pore structure of $FeNi_3$/NCS were studied by N_2 adsorption and desorption experiments (Fig. S9†). $FeNi_3$/NCS shows a type-IV isotherm, indicating the existence of mesopores. The pore-size distribution plot further corroborates the presence of mesopores, yet the macropores may result from the stacking of the sample. The specific surface area and the maxima pore size were calculated to be 33.35 $m^2\ g^{-1}$ and 19.2 nm, in line with the porous features of LDHs and their derivatives.[41,58]

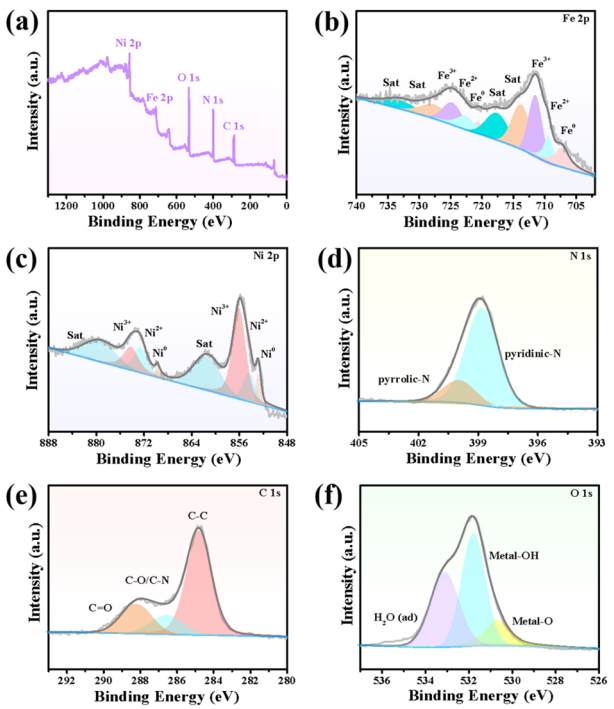

Fig. 2 (a) Full survey XPS spectrum and high-resolution XPS spectra of (b) Fe 2p (c) Ni 2p, (d) N 1s, (e) C 1s, and (f) O 1s of $FeNi_3$/NCS.

3.2 OER performance of the $FeNi_3$/NCS electrocatalyst

The electrocatalytic activity of $FeNi_3$/NCS towards the OER was first evaluated in O_2-saturated 1.0 M KOH solution. For comparison, NCT (calcined from the melamine tube), FeNiO/C (calcined from FeNi-LDH) and RuO_2 were tested under similar conditions. In addition, the OER polarization curves of FeNi/NC obtained from the pyrolysis of the mixture of melamine tube and FeNi-LDH, and the precursor of Mel-T@FeNi-LDH were also measured. Fig. 3a plots the LSV curves of the as-prepared samples, where the $FeNi_3$/NCS electrocatalyst exhibits the smallest onset potential and overpotential ($E_{j=10}$) at a current density of 10 mA cm^{-2}. The $E_{j=10}$ values of the tested samples have the following order: $FeNi_3$/NCS (260 mV) < RuO_2 (300 mV) < FeNi/NC (340 mV) < FeNiO/C (420 mV) < Mel-T@FeNi-LDH (570 mV) ≪ NCT (>700 mV) (Fig. S10†). The highest OER catalytic activity of $FeNi_3$/NCS should be primarily designated to the synergistic effect of $FeNi_3$ NPs and the N-doped nanosheets (NCS) as compared with the poor performance of FeNiO/C and NCT. The strong interfacial electronic coupling between $FeNi_3$ and NCS is reflected by XPS (Fig. S11†), where the binding energies of Ni 2p and Fe 2p for $FeNi_3$/NCS are up-shifted

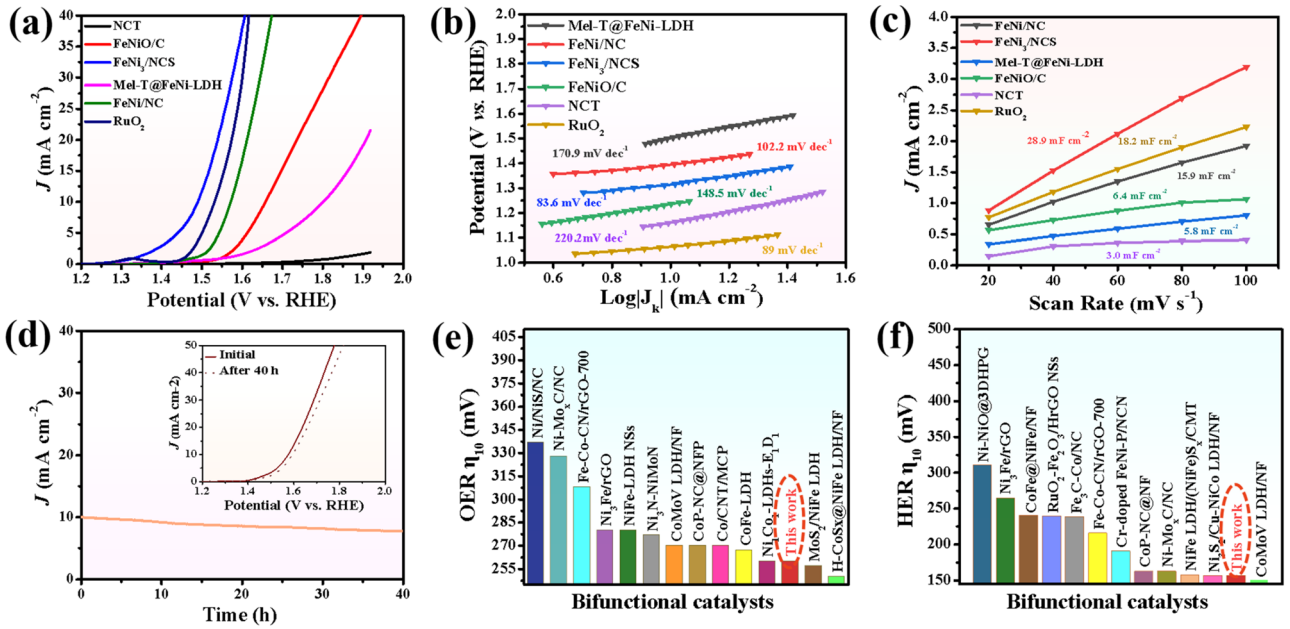

Fig. 3 (a) OER LSV profiles, (b) Tafel slopes, and (c) C_{dl} of $FeNi_3$/NCS, NCT, FeNiO/C, FeNi/NC, Mel-T@FeNi-LDH and RuO_2. (d) Amperometric *i*–*t* of $FeNi_3$/NCS at 10 mA cm^{-2} (inset: the polarization curve of $FeNi_3$/NCS after *i*–*t* measurement); comparison of (e) OER and (f) HER overpotential of this work and reported FeNi-containing electrocatalysts.

compared to those of FeNiO/C, thus leading to improved electrocatalytic activity by locally modifying the electronic structure of the interfacial active sites.[5,59,60] Particularly, the undesirable performance of FeNi/NC compared with $FeNi_3$/NCS illustrates the advance of the fabrication strategy for the $FeNi_3$/NCS electrocatalyst, that is, the combination of hydrothermal and the low-temperature pyrolysis methods, enabling the uniformly dispersed active species than the physical mixture. As shown in Fig. 3b, the Tafel slope of $FeNi_3$/NCS is 83.6 mV dec^{-1}, which is smaller than that of FeNiO/C (148.5 mV dec^{-1}), NCT (220.2 mV dec^{-1}), FeNi/NC (102.2 mV dec^{-1}), Mel-T@FeNi-LDH (170.9 mV dec^{-1}) and even the commercial RuO_2 (89 mV dec^{-1}). The small Tafel slope of $FeNi_3$/NCS indicates that the introduction of $FeNi_3$ NPs into N-doped carbon nanosheets has expedited the catalytic reaction. Electrochemical impedance spectroscopy (EIS) was performed to further investigate the OER kinetics. As shown in Fig. S12a,† the $FeNi_3$/NCS has the smallest semicircle radius, and the charge transfer resistance (R_{ct}) value is 12.48 Ω, while the R_{ct} values of FeNiO/C, NCT, FeNi/NC, Mel-T@FeNi-LDH and RuO_2 are 66.7, 70.7, 49.5, 67.8 and 41.8 Ω. The small R_{ct} of $FeNi_3$/NCS suggests fast kinetics and superior electrocatalytic activity for the OER.[61] To further unveil the underlying reason for the catalytic activity, electrochemically active surface area (ECSA) was investigated by determining the capacitance (C_{dl}) owing to the linear relationship between ECSA and C_{dl} for similar samples measured in the identical electrolyte.[62,63] The C_{dl} value was measured *via* the cyclic voltammetry (CV) method at different scan rates (Fig. S13†) in a potential range without an apparent faradaic process. C_{dl} is determined from the equation of $C_{dl} = i_c/v$, where i_c is the current density and v is the scan rate.[64] As shown in Fig. 3c, $FeNi_3$/NCS has a C_{dl} value of 28.9 mF cm^{-2}, significantly larger than that of FeNiO/C (6.4 mF cm^{-2}), FeNi/NC (15.9 mF cm^{-2}), Mel-T@FeNi-LDH (5.8 mF cm^{-2}) and NCT (3.0 mF cm^{-2}). The large C_{dl} value corroborates the large ECSA, thus providing higher inherent electrocatalytic active sites.[65] In addition, the intrinsic OER catalytic activities of the electrodes are evaluated using the turnover frequency (TOF),[66] assuming that all metal atoms are catalytically active. As shown in Fig. S12b,† the much higher TOF value of $FeNi_3$/NCS (0.515 s^{-1}) compared to the corresponding references (*i.e.*, RuO_2 (0.227 s^{-1}), FeNi/NC (0.222 s^{-1}), FeNiO/C (0.103 s^{-1}), Mel-T@FeNi-LDH (0.079 s^{-1}), and NCT (0.043 s^{-1})) further verified the excellent OER performance of $FeNi_3$/NCS. The long-term stability of $FeNi_3$/NCS was measured by the amperometric *i*–*t* test as shown in Fig. 3d. There is no obvious change of current density during continuous working for 40 h, and only a weak potential decay (19 mV) at 10 mA cm^{-2}. The results imply the remarkable durability of $FeNi_3$/NCS during the OER. The outstanding stability of the $FeNi_3$/NCS was further confirmed by TEM, XRD and XPS analysis after the OER stability test. Fig. S14a and S14c† show that there is no obvious change in both the morphology and crystal structure after the long-time test. In addition, the Ni 2p XPS analysis demonstrates that the Ni^{2+} peaks after the OER shift to higher binding energy and Ni^0 peaks disappear (Fig. S15a†). Analogously, the peaks of Fe^{2+} shift to higher binding energy and Fe^0 peaks disappear (Fig. S15b†), indicating partial surface oxidation of $FeNi_3$/NCS.[67,68] Meanwhile, the partial surface oxidation of $FeNi_3$/NCS during the OER stability test is also reflected by the O 1s spectrum, where the M–O intensity increased obviously (Fig. S15c†). The Raman spectrum of the $FeNi_3$/NCS electrocatalyst after the stability test was measured to certify the formation of metallic

oxyhydroxides. As shown in Fig. S15d,† the emerging peaks at about 481 cm^{-1} and 648 cm^{-1} are assigned to NiOOH and FeOOH, indicating the formation of metallic oxyhydroxides during the OER process.[69–72] Fig. 3e compares the OER overpotential of $FeNi_3$/NCS with previously reported FeNi-containing OER catalysts (from Table S1†). It is seen that the OER activity of $FeNi_3$/NCS is comparable to and even superior to that of the reported catalysts.

3.3 HER performance of the $FeNi_3$/NCS electrocatalyst

The electrocatalytic activity of $FeNi_3$/NCS towards the HER was scrutinized in N_2-saturated 1.0 M KOH solution and compared with the benchmark Pt/C. Fig. 4a indicates that $FeNi_3$/NCS exhibits better HER activity than NCT, FeNiO/C, FeNi/NC, and Mel-T@FeNi-LDH. The overpotential of the measured samples is plotted in Fig. S16a.† Notably, the Tafel slope of $FeNi_3$/NCS (99.5 mV dec^{-1}) is lower than that of the references of NCT (183.1 mV dec^{-1}), FeNi/NC (102.6 mV dec^{-1}), Mel-T@FeNi-LDH (291.7 mV dec^{-1}) and FeNiO/C (157.1 mV dec^{-1}) (Fig. 4b), signifying the favorable HER kinetics of $FeNi_3$/NCS. The EIS measurement demonstrates that the electron transfer kinetics and conductivity of $FeNi_3$/NCS are superior to those of NCT and FeNiO/C, and even close to that of Pt/C (Fig. S16b†). As shown in Fig. 4c and S17,† $FeNi_3$/NCS has much larger C_{dl} (24.7 mF cm^{-2}) than NCT (3.9 mF cm^{-2}), Mel-T@FeNi-LDH (2.1 mF cm^{-2}), FeNiO/C (7.2 mF cm^{-2}), and FeNi/NC (20.7 mF cm^{-2}), suggesting more electrochemically active sites and better HER activity.[6] The remarkably increased HER activity of $FeNi_3$/NCS over NCT and FeNiO/C primarily stems from the synergistic effect of $FeNi_3$ and N-doped carbon nanosheets. In addition, the decorated $FeNi_3$ on the 2D nanosheets provides numerous accessible active sites as well as an efficient mass/electron transfer pathway. The current density of $FeNi_3$/NCS is slightly changed (Fig. 4d) and only negligible potential change (15 mV) emerges during 40 h electrolysis (inset Fig. 4d), substantiating the excellent stability of $FeNi_3$/NCS towards the HER. The high HER stability of $FeNi_3$/NCS is also demonstrated by the negligible variation of the morphology and crystal structure (Fig. S14b and S14c†). The comparison between this work and previous studies on the HER performance is demonstrated in Fig. 3f, indicating the competitive HER performance of $FeNi_3$/NCS among various literature reported catalysts (Table S2†).

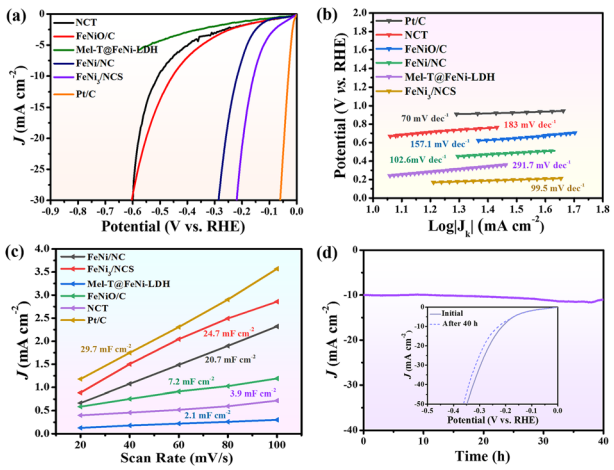

Fig. 4 (a) HER LSV profiles, (b) Tafel slopes, (c) C_{dl} of NCT, FeNiO/C, FeNi/NC, Mel-T@FeNi-LDH, $FeNi_3$/NCS, and Pt/C. (d) Amperometric *i*–*t* curve of $FeNi_3$/NCS at 10 mA cm^{-2} (inset: the polarization curve of $FeNi_3$/NCS after *i*–*t* measurement).

3.4 Effect of pyrolysis temperature on OER/HER performance

As the pyrolysis temperature has an evident influence on the electrocatalytic activity of the carbon materials, we examined the pyrolysis of Mel-T@FeNi-LDH at different temperatures. As FeNi-LDH starts to decompose at around 300 °C (Fig. S18†), 350 °C, 400 °C and 450 °C were chosen as the representative temperatures. As shown in Fig. S19a,† the Mel-T@FeNi-LDH converts into smooth nanosheets after pyrolysis at 350 °C for 2 h. With increasing the carbonized temperature from 350 °C to 400 °C and 450 °C, the surface of the carbon nanosheets becomes coarser (Fig. S19b and c†). The TEM images at different pyrolysis temperatures are presented in Fig. 5a–c. The carbon nanosheets embedded with nanoparticles are observed at 350 °C, while dense metal NPs are uniformly implanted when the temperature increased to 400 °C. On further increasing to 450 °C, much bigger metal NPs with obvious aggregation are observed, accompanied by the gradual disappearance of carbon nanosheets. XRD was employed to characterize the crystal structure of the resultant samples. As shown in Fig. 5d, the carbonized sample obtained at 350 °C (S-350) exhibits obvious peaks of the (021) plane of Fe_3O_4 and (220) plane of NiO.[52,67] Distinguishable $FeNi_3$ NPs peaks with relatively weak Ni peaks are observed after pyrolysis at 400 °C. The $FeNi_3$ NP characteristic peaks are intensified at 450 °C. Thus, it is reasonable to infer that the Mel-T@FeNi-LDH starts to decompose and transforms into metal oxide encapsulated carbon nanosheets at a lower temperature (*i.e.*, 350 °C), which are alloyed into $FeNi_3$ NP implanted carbon nanosheets at 400 °C. The $FeNi_3$ NPs evolved into bigger and aggregated particles at 450 °C owing to the gradual loss of the carbon matrix.

The OER and HER catalytic activity of Mel-T@FeNi-LDH pyrolyzed at different temperatures were then examined. As shown in Fig. 5e, the sample calcined at 400 °C (S-400) shows the best OER activity with a low overpotential of 260 mV, outperforming the samples calcined at 350 °C (S-350) and 450 °C (S-450). Similarly, S-400 delivers more favorable HER activity than S-350 and S-450 (Fig. 5f and S20a†). The higher catalytic activity of S-400 can be attributed to the well-balanced conductivity and the efficient active sites. Apparently, the active $FeNi_3$ alloy has not formed at 350 °C, and some products are still in the amorphous state, while at 450 °C, the large particle size can reduce the effective active areas. The EIS measurement and the capacitance (C_{dl}) were further calculated to illustrate the different catalytic activities. As shown in Fig. S20b,† S-400 has the smallest semicircle radius, and the R_{ct} is 12.48 Ω, while S-350 and S-450 have much larger R_{ct} of 52.57 Ω and 25.54 Ω. The C_{dl} of S-350, S-400, and S-450 is determined to be 8.1 mF cm^{-2}, 28.9 mF cm^{-2}, and 14.3 mF cm^{-2}, respectively (Fig. S20c and

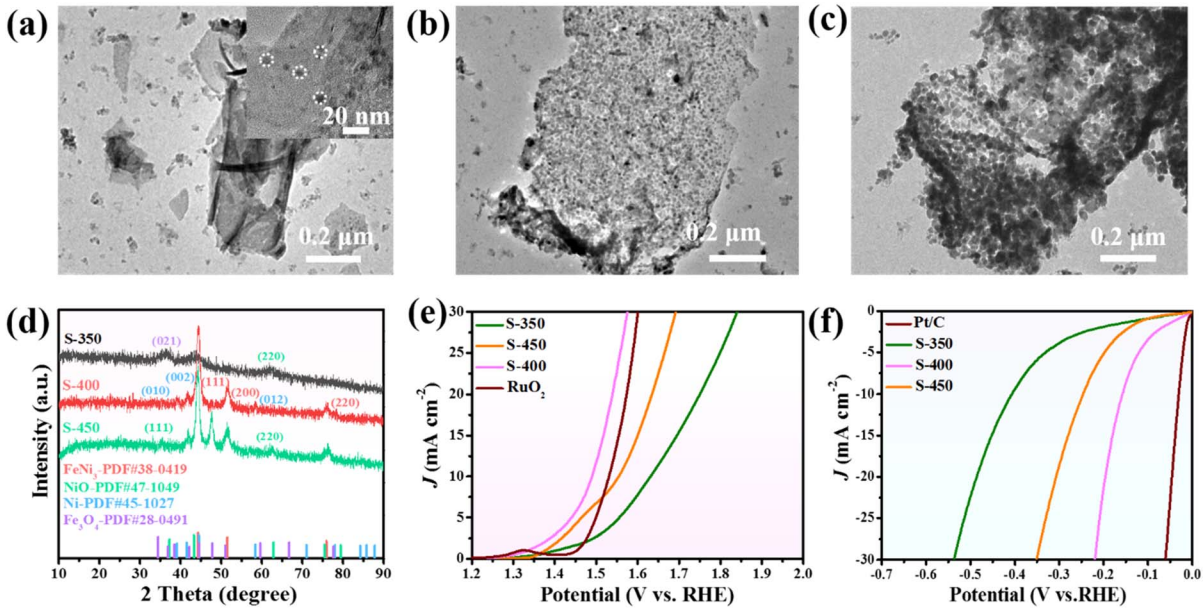

Fig. 5 TEM images of Mel-T@FeNi-LDH after pyrolysis at (a) 350 °C, (b) 400 °C, and (c) 450 °C for 2 h; (d) XRD patterns, (e) OER and (f) HER LSV profiles of the carbonized samples.

S21†). As expected, such a low R_{ct} and a high C_{dl} enable the optimal catalytic activity of S-400, which is denoted as the $FeNi_3$/NCS electrocatalyst in this work.

3.5 DFT calculations

DFT simulation was employed to investigate the underlying electrocatalytic mechanism. To better illustrate the synergistic effect in $FeNi_3$/NCS, the theoretical models of N-doped carbon nanosheets (NCS), $FeNi_3$ and $FeNi_3$/NCS are built and shown in Fig. 6a. Generally, the OER pathway in the alkaline solution involves four steps:[68] (i) creation of OH*, (ii) formation of O*, (iii) generation of OOH*, and (iv) release of O_2, and the corresponding models are presented in Fig. S22.† The Gibbs free energy change (ΔG) of each elementary step in the OER process is usually used to evaluate the electrocatalytic activity of the catalyst, and the step with a maximum ΔG value represents the rate-determining step (RDS). Theoretically, the OER electrocatalytic activity is strongly dependent on the ΔG_{rds} on the surface of the electrocatalyst, and a smaller ΔG_{rds} indicates faster OER reaction kinetics.[73] As shown in Fig. 6b and Fig. S23,† the RDS of NCS is the formation of OH* at the applied potentials (*i.e.*, $U = 1.23$ V and $U = 0$ V), and the RDS of $FeNi_3$ and $FeNi_3$/NCS is the formation of OOH* from O*. After 1.23 V potential was applied to the system, the ΔG_{OH^*} of NCS is 0.49 eV, the ΔG_{OOH^*} of $FeNi_3$ is 0.38 eV, and the ΔG_{OOH^*} of $FeNi_3$/NCS is 0.28 eV. The significantly decreased ΔG_{rds} of $FeNi_3$/NCS indicates a faster catalytic kinetics and better catalytic activity caused by the combination of $FeNi_3$ and N-doped carbon nanosheets in $FeNi_3$/NCS.

For the HER under alkaline conditions, the two steps of (i) Volmer reaction: $H_2O + * + e^- \rightarrow H^* + OH^-$; (ii) Heyrovsky reaction: $H^* + H_2O + e^- \rightarrow H_2 + OH^-$, or Tafel reaction: $H^* + H^* \rightarrow H_2$ are included. The well-recognized activity of the catalyst is related to the absorption free energy of the hydrogen intermediate H* (ΔG_{H^*}). The optimal value of ΔG_{H^*} is close to zero.[68,74] For a selected catalyst, a suitable ΔG_{H^*} value (*i.e.*, close to zero) means an appropriate H binding strength, which is not only conducive to the adsorption of H, accelerating the transfer of electrons, but also beneficial to the desorption of H_2 from the catalyst surface, thus indicating the high HER intrinsic activity.[75] The configurations of absorption of H* are presented in Fig. S24† and the absorption energy is shown in Fig. 6c. The ΔG_{H^*} values of NCS, $FeNi_3$, and $FeNi_3$/NCS are 0.30, 0.25, and 0.12 eV, respectively. The obviously reduced ΔG_{H^*} value of $FeNi_3$/NCS indicates that $FeNi_3$/NCS can accelerate the HER kinetics, thereby improving the HER electrocatalytic activity.

In addition, the electron density difference between $FeNi_3$/NCS and NCS is shown in Fig. 6d; the yellow region indicates fewer electrons and the blue region demonstrates electron accumulation. Clearly, electrons are transferred from $FeNi_3$ to N-doped carbon, affording a charge-rich state on the N-doped carbon and thus leading to better catalytic activity of $FeNi_3$/NCS. Fig. 6e shows the density of states (DOS) of $FeNi_3$/NCS, and the electron density is obviously increased compared with the pristine NCS, suggesting that the $FeNi_3$ decorated NCS can release more electrons to participate in the OER process.[76] Therefore, the enhanced OER/HER activity of $FeNi_3$/NCS is mainly assigned to the decreased free energy barriers and accelerated electron transfer kinetics, which possibly originates from the synergistic effect of $FeNi_3$ and NCS.

3.6 Overall water splitting

The prominent OER and HER catalytic activity of $FeNi_3$/NCS trigger the practical application in electrocatalytic water splitting. The two-electrode electrolytic cell was assembled by using $FeNi_3$/NCS as both the cathode and anode catalyst in 1.0 M KOH

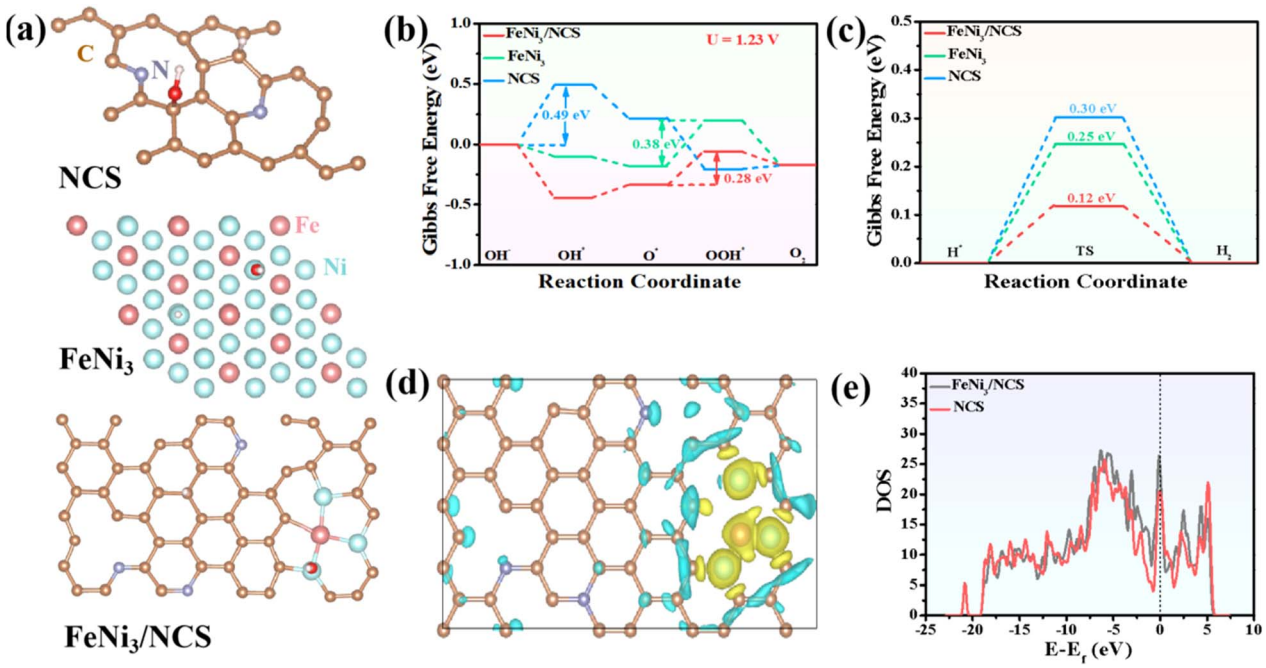

Fig. 6 (a) Structure models of NCS, $FeNi_3$, and $FeNi_3$/NCS used for DFT calculation. (b) The Gibbs free energy diagrams of NCS, $FeNi_3$, and $FeNi_3$/NCS for the OER. (c) The Gibbs free energies of H* on the surfaces of NCS, $FeNi_3$, and $FeNi_3$/NCS. (d) Electron density difference between $FeNi_3$/NCS and NCS (the yellow region represents fewer electrons and the blue region represents more electrons). (e) The density of states (DOS) for NCS and $FeNi_3$/NCS.

solution. Fig. 7a presents the polarization curves of the $FeNi_3$/NCS (+‖−), NCT (+‖−), FeNiO/C (+‖−), and RuO_2–Pt/C (+‖−) electrodes for overall water splitting at a scan rate of 5 mV s^{-1}. To reach a current density of 10 mA cm^{-2}, the $FeNi_3$/NCS (+‖−) electrode needs a cell voltage of 1.53 V, which is significantly lower than that of the FeNiO/C (+‖−) electrode (1.82 V) and NCT (+‖−) electrode. Impressively, the $FeNi_3$/NCS (+‖−) electrode outperforms the benchmark RuO_2–Pt/C (+‖−) electrode, which requires a voltage of 1.56 V to reach a current density of 10 mA cm^{-2}. Furthermore, Fig. 7b describes the experimental and theoretical volumes of H_2 and O_2 from the assembled electrolytic cell at $J = 10$ mA cm^{-2}. The collected gases matched well with the calculated amounts (inset of Fig. 7c) and high faradaic efficiencies for O_2 (90%) and H_2 (98%) are achieved. The long-term overall water-splitting stability is evaluated by chronoamperometry. As shown in Fig. 7c, there is negligible current loss during 12 h of electrolysis at 10 mA cm^{-2}, implying excellent overall water-splitting stability of $FeNi_3$/NCS. Fig. 7d compares the cell voltages of various water-splitting devices based on FeNi-containing electrocatalysts. The catalytic performance of $FeNi_3$/NCS prepared in this work is comparable to or even much better than previous studies (Table S3†).

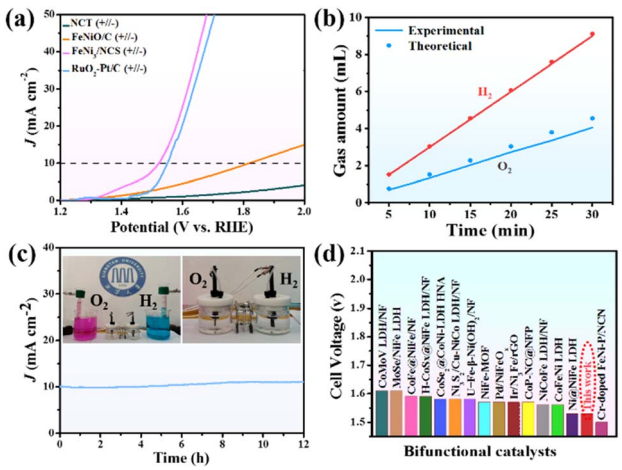

Fig. 7 (a) Overall water-splitting performance of NCT (+‖−), FeNiO/C (+‖−), $FeNi_3$/NCS (+‖−), and RuO_2–Pt/C (+‖−) with a scan rate of 5 mV s^{-1}; (b) the collected and theoretical H_2 and O_2 volumes at a fixed current density of 10 mA cm^{-2}; (c) the long-term durability at a current density of 10 mA cm^{-2}, and the inset is the photograph of the assembled electrolytic cell; (d) comparison of the overall water-splitting performance of this work and previous reports.

4. Conclusions

In summary, we have proposed a combination strategy of hydrothermal reaction and low-temperature pyrolysis to craft $FeNi_3$ NP embedded N-doped carbon nanosheets (denoted as $FeNi_3$/NCS) as an efficient OER/HER bifunctional electrocatalyst for overall water splitting. A melamine tube was employed as a self-supporting template to generate FeNi-LDH by a hydrothermal method, yielding the core–shell structured Mel-T@FeNi-LDH. The $FeNi_3$/NCS catalyst was produced by low-temperature pyrolysis of Mel-T@FeNi-LDH, and the influence of pyrolysis temperature on the electrocatalytic activity of the

resultant samples was systematically investigated. $FeNi_3$/NCS demonstrated outstanding OER and HER activity and durability in alkaline electrolyte. Both the OER (260 mV) and HER (156 mV) overpotentials of $FeNi_3$/NCS were significantly lower than those of NCT (>700 *vs.* 510 mV) and FeNiO/C (420 *vs.* 440 mV), signifying the crucial role of the synergistic effect between $FeNi_3$ and N-doped carbon nanosheets on the largely enhanced bifunctional activity. DFT calculations further confirmed that the greatly boosted OER/HER activity was related to the decreased free energy barriers and accelerated electron transfer kinetics in $FeNi_3$/NCS. By using $FeNi_3$/NCS as the cathodic and anodic catalyst to assemble the electrolytic cell for water splitting, a small cell voltage of 1.53 V was achieved at 10 mA cm^{-2}, superior to the benchmark RuO_2–Pt/C (+‖−) (1.56 V) and greatly outperforming the counterpart NCT and FeNiO/C-based devices. Compared with the developed FeNi-containing electrocatalysts, $FeNi_3$/NCS exhibited unambiguously comparable and even better catalytic activity. The design and preparation method developed in this work may promote the promising application of LDHs and their derivatives in the field of energy conversion and storage technologies.

Author contributions

Rong Xin: investigation, data analysis, validation, writing – original draft. Yijiang Liu: supervision, methodology, data analysis, validation, writing – review& editing, funding acquisition. Xuxin Li: data analysis, validation. Shicheng Yi: data analysis, validation. Mingyue Zhang: data analysis, validation. Hongbiao Chen: data analysis, validation. Huaming Li: data analysis, validation. Zhiqun Lin: methodology, data analysis, validation, writing – review& editing.

Conflicts of interest

The authors declare that they have no known competing financial interests or personal relationships that could have appeared to influence the work reported in this paper.

Acknowledgements

This work was supported by the National Natural Science Foundation of China (52173207), the Science Fund for Distinguished Young Scholars of Hunan Province of China (2023JJ10040), the Science and Technology Innovation Program of Hunan Province (2022RC1077), and the Outstanding Youth Fund Project of Hunan Provincial Department of Education (21B0119).

Notes and references

1 J. McAllister, N. A. G. Bandeira, J. C. McGlynn, A. Y. Ganin, Y. F. Song, C. Bo and H. N. Miras, *Nat. Commun.*, 2019, **10**, 370–379.
2 H. Song, S. Luo, H. Huang, B. Deng and J. Ye, *ACS Energy Lett.*, 2022, **7**, 1043–1065.
3 G. Song, S. Luo, Q. Zhou, J. Zou, Y. Lin, L. Wang, G. Li, A. Meng and Z. Li, *J. Mater. Chem. A*, 2022, **10**, 18877–18888.
4 Y. Bai, H. Y. Zhang, X. Lu, L. Wang, Y. Zou, J. H. Miao, M. Qiao, Y. J. Tang and D. D. Zhu, *Chem.–Eur. J.*, 2023, e202300205–e202300211.
5 Y. J. Lee and S. K. Park, *Small*, 2022, **18**, 2200586.
6 H. Y. Zhang, B. Li, Y. Zou, J. H. Miao, M. Qiao, Y. J. Tang, X. Zhang and D. D. Zhu, *Chem. Commun.*, 2022, **58**, 8556–8559.
7 Y. Yan, B. Y. Xia, B. Zhao and X. Wang, *J. Mater. Chem. A*, 2016, **4**, 17587–17603.
8 C. Hu, R. Paul, Q. Dai and L. Dai, *Chem. Soc. Rev.*, 2021, **50**, 11785–11843.
9 W. J. Jiang, T. Tang, T. Tang, Y. Zhang, J. S. Hu and J. S. Hu, *Acc. Chem. Res.*, 2020, **53**, 1111–1123.
10 Y. Cheng, H. Guo, P. Yuan, X. Li, L. Zheng and R. Song, *Chem. Eng. J.*, 2021, **413**, 127531.
11 W. Jiang, A. Y. Faid, B. F. Gomes, I. Galkina, L. Xia, C. M. S. Lobo, M. Desmau, P. Borowski, H. Hartmann, A. Maljusch, A. Besmehn, C. Roth, S. Sunde, W. Lehnert and M. Shviro, *Adv. Funct. Mater.*, 2022, **32**, 2203520.
12 X. Zou and Y. Zhang, *Chem. Soc. Rev.*, 2015, **44**, 5148–5180.
13 K. Shah, R. Dai, M. Mateen, Z. Hassan, Z. Zhuang, C. Liu, M. Israr, W. C. Cheong, B. Hu and R. Tu, *Angew. Chem.*, 2022, **134**, e202114951.
14 T. Wang, P. Wang, W. Zang, X. Li, D. Chen, Z. Kou, S. Mu and J. Wang, *Adv. Funct. Mater.*, 2022, **32**, 2107382.
15 T. I. Singh, G. Rajeshkhanna, U. N. Pan, T. Kshetri, H. Lin, N. H. Kim and J. H. Lee, *Small*, 2021, **17**, 2101312.
16 Y. Zhang, X. Xia, X. Cao, B. Zhang, N. H. Tiep, H. He, S. Chen, Y. Huang and H. J. Fan, *Adv. Energy Mater.*, 2017, **7**, 1700220.
17 L. Xiu, Z. Wang, M. Yu, X. Wu and J. Qiu, *ACS Nano*, 2018, **12**, 8017–8028.
18 Z. Kou, T. Wang, Q. Gu, M. Xiong, L. Zheng, X. Li, Z. Pan, H. Chen, F. Verpoort, A. K. Cheetham, S. Mu and J. Wang, *Adv. Energy Mater.*, 2019, **9**, 1803768.
19 Y. Yu, J. Zhou and Z. Sun, *Adv. Funct. Mater.*, 2020, **30**, 2000570.
20 P. Chen, J. Ye, H. Wang, L. Ouyang and M. Zhu, *J. Alloys Compd.*, 2021, **883**, 160833.
21 N. Han, P. Liu, J. Jiang, L. Ai, Z. Shao and S. Liu, *J. Mater. Chem. A*, 2018, **6**, 19912–19933.
22 Z. Liu, D. Liu, L. Zhao, J. Tian, J. Yang and L. Feng, *J. Mater. Chem. A*, 2021, **9**, 7750–7758.
23 Y. Guo, T. Park, J. W. Yi, J. Henzie, J. Kim, Z. Wang, B. Jiang, Y. Bando, Y. Sugahara, J. Tang and Y. Yamauchi, *Adv. Mater.*, 2019, **31**, 1807134.
24 M. Yan, Z. Zhao, P. Cui, K. Mao, C. Chen, X. Wang, Q. Wu, H. Yang, L. Yang and Z. Hu, *Nano Res.*, 2021, **14**, 4220–4226.
25 M. Wang, L. Zhang, Y. He and H. Zhu, *J. Mater. Chem. A*, 2021, **9**, 5320–5363.
26 Y. J. Tang, Y. Zou and D. D. Zhu, *J. Mater. Chem. A*, 2022, **10**, 12438–12446.
27 Y. Liu, Z. Zhang, L. Zhang, Y. Xia, H. Wang, H. Liu, S. Ge and J. Yu, *J. Mater. Chem. A*, 2022, **10**, 22125–22134.
28 H. Zhang, A. W. Maijenburg, X. Li, S. L. Schweizer and R. B. Wehrspohn, *Adv. Funct. Mater.*, 2020, **30**, 2003261.

29 H. You, D. Wu, D. Si, M. Cao, F. Sun, H. Zhang, H. Wang, T.-F. Liu and R. Cao, *J. Am. Chem. Soc.*, 2022, **144**, 9254–9263.
30 Y. Zhu, Q. Lin, Y. Zhong, H. A. Tahini, Z. Shao and H. Wang, *Energy Environ. Sci.*, 2020, **13**, 3361–3392.
31 L. Lei, D. Huang, C. Zhou, S. Chen, X. Yan, Z. Li and W. Wang, *Coord. Chem. Rev.*, 2020, **408**, 213177.
32 Y. Sun, T. Zhang, C. Li, K. Xu and Y. Li, *J. Mater. Chem. A*, 2020, **8**, 13415–13436.
33 D. Zhou, P. Li, X. Lin, A. McKinley, Y. Kuang, W. Liu, W. F. Lin, X. Sun and X. Duan, *Chem. Soc. Rev.*, 2021, **50**, 8790–8817.
34 P. M. Bodhankar, P. B. Sarawade, G. Singh, A. Vinu and D. S. Dhawale, *J. Mater. Chem. A*, 2021, **9**, 3180–3208.
35 Y. Wang, D. Yan, S. El Hankari, Y. Zou and S. Wang, *Adv. Sci.*, 2018, **5**, 1800064.
36 X. Li, C. Liu, Z. Fang, L. Xu, C. Lu and W. Hou, *J. Mater. Chem. A*, 2022, **10**, 20626–20634.
37 H. S. Chavan, C. H. Lee, A. I. Inamdar, J. Han, S. Park, S. Cho, N. K. Shreshta, S. U. Lee, B. Hou, H. Im and H. Kim, *ACS Catal.*, 2022, **12**, 3821–3831.
38 R. Keyikoglu, A. Khataee, H. Lin and Y. Orooji, *Chem. Eng. J.*, 2022, **434**, 134730.
39 L. Yang, D. Xu, H. Yang, X. Luo and H. Liang, *Chem. Eng. J.*, 2022, **432**, 134436.
40 X. Teng, L. Guo, L. Ji, J. Wang, Y. Niu, Z. Hu and Z. Chen, *ACS Appl. Energy Mater.*, 2019, **2**, 5465–5471.
41 F. Du, J. Li, C. Wang, J. Yao, Z. Tan, Z. Yao, C. Li and C. Guo, *Chem. Eng. J.*, 2022, **434**, 134641.
42 Y. Chen, H. Yao, F. Kong, H. Tian, G. Meng, S. Wang, X. Mao, X. Cui, X. Hou and J. Shi, *Appl. Catal. B Environ.*, 2021, **297**, 120474.
43 K. Zheng, J. Ren, X. Li, G. Li, L. Jiao and C. Xu, *Chem. Eng. J.*, 2022, **441**, 136031.
44 A. Hameed, M. Batool, Z. Liu, M. A. Nadeem and R. Jin, *ACS Energy Lett.*, 2022, **7**, 3311–3328.
45 Y. Ma, D. Liu, H. Wu, M. Li, S. Ding, A. S. Hall and C. Xiao, *ACS Appl. Mater. Interfaces*, 2021, **13**, 26055–26063.
46 Y. Wang, S. Wang, Z.-L. Ma, L.-T. Yan, X.-B. Zhao, Y.-Y. Xue, J.-M. Huo, X. Yuan, S.-N. Li and Q.-G. Zhai, *Adv. Mater.*, 2022, **34**, 2107488.
47 T. Wang, Y. He, Y. Liu, F. Guo, X. Li, H. Chen, H. Li and Z. Lin, *Nano Energy*, 2021, **79**, 105487.
48 X. Li, Y. Liu, H. Chen, M. Yang, D. Yang, H. Li and Z. Lin, *Nano Lett.*, 2021, **21**, 3098–3105.
49 Y. Li, Y.-C. Miao, C. Yang, Y.-X. Chang, Y. Su, H. Yan and S. Xu, *Chem. Eng. J.*, 2023, **451**, 138548.
50 Z. Liu, S. Li, F. Wang, M. Li and Y. Ni, *Dalton Trans.*, 2021, **50**, 6306–6314.
51 D. Chen, J. Zhu, X. Mu, R. Cheng, W. Li, S. Liu, Z. Pu, C. Lin and S. Mu, *Appl. Catal. B Environ.*, 2020, **268**, 118729.
52 K. Srinivas, Y. Lu, Y. Chen, W. Zhang and D. Yang, *ACS Sustain. Chem. Eng.*, 2020, **8**, 3820–3831.
53 H. Chen, Y. Liu, B. Liu, M. Yang, H. Li and H. Chen, *Nanoscale*, 2022, **14**, 12431–12436.
54 L. Jia, G. Du, D. Han, Y. Hao, W. Zhao, Y. Fan, Q. Su, S. Ding and B. Xu, *J. Mater. Chem. A*, 2021, **9**, 27639–27650.
55 T. Wang, C. Yang, Y. Liu, M. Yang, X. Li, Y. He, H. Li, H. Chen and Z. Lin, *Nano Lett.*, 2020, **20**, 5639–5645.
56 F. Guo, M. Zhang, S. Yi, X. Li, R. Xin, M. Yang, B. Liu, H. Chen, H. Li and Y. Liu, *Nano Res. Energy*, 2022, **1**, e9120027.
57 X. Cai, X. Shen, L. Ma, Z. Ji, C. Xu and A. Yuan, *Chem. Eng. J.*, 2015, **268**, 251–259.
58 X. Feng, Q. Jiao, W. Chen, Y. Dang, Z. Dai, S. L. Suib, J. Zhang, Y. Zhao, H. Li and C. Feng, *Appl. Catal. B Environ.*, 2021, **286**, 119869.
59 Q. Yang, Q. Xu and H. L. Jiang, *Chem. Soc. Rev.*, 2017, **46**, 4774–4808.
60 X. P. Li, L. R. Zheng, S. J. Liu, T. Ouyang, S. Ye and Z. Q. Liu, *Chin. Chem. Lett.*, 2022, **33**, 4761–4765.
61 N. Wang, S. Ning, X. Yu, D. Chen, Z. Li, J. Xu, H. Meng, D. Zhao, L. Li, Q. Liu, B. Lu and S. Chen, *Appl. Catal. B Environ.*, 2022, **302**, 120838.
62 C. C. Yang, S. F. Zai, Y. T. Zhou, L. Du and Q. Jiang, *Adv. Funct. Mater.*, 2019, **29**, 1901949.
63 H. Deng, C. Zhang, Y. Xie, T. Tumlin, L. Giri, S. P. Karna and J. Lin, *J. Mater. Chem. A*, 2016, **4**, 6824–6830.
64 C. C. L. McCrory, S. Jung, J. C. Peters and T. F. Jaramillo, *J. Am. Chem. Soc.*, 2013, **135**, 16977–16987.
65 E. Pajootan, S. Omanovic and S. Coulombe, *Chem. Eng. J.*, 2021, **426**, 131706.
66 S. Anantharaj and S. Kundu, *ACS Energy Lett.*, 2019, **4**, 1260–1264.
67 G. Koçak, V. Bütün and C. Tuncer, *J. Appl. Polym. Sci.*, 2021, **138**, 51299.
68 Y. N. Guo, T. Park, J. W. Yi, J. Henzie, J. H. Kim, Z. L. Wang, B. Jiang, Y. Bando, Y. Sugahara, J. Tang and Y. Yamauchi, *Adv. Mater.*, 2019, **31**, 1807134.
69 H. Yang, L. Q. Gong, H. M. Wang, C. L. Dong, J. L. Wang, K. Qi, H. F. Liu, X. P. Guo and B. Y. Xia, *Nat. Commun.*, 2020, **11**, 5075.
70 W. F. Peng, J. K. Li, K. Q. Shen, L. R. Zheng, H. Tang, Y. T. Gong, J. S. Zhou, N. Chen, S. J. Zhao, M. Y. Chen, F. M. Gao and H. Y. Gou, *J. Mater. Chem. A*, 2012, **8**, 23580–23589.
71 A. C. Garcia, T. Touzalin, C. Nieuwland, N. Perini and M. T. M. Koper, *Angew. Chem., Int. Ed.*, 2019, **58**, 12999–13003.
72 M. W. Louie and A. T. Bell, *J. Am. Chem. Soc.*, 2013, **135**, 12329–12337.
73 L. Peng, J. Wang, Y. Nie, K. Xiong, Y. Wang, L. Zhang, K. Chen, W. Ding, L. Li and Z. Wei, *ACS Catal.*, 2017, **7**, 8184–8191.
74 M. Yang, Y. M. Jiang, M. J. Qu, Y. C. Qin, Y. Wang, W. Shen, R. X. He, W. Su and M. Lia, *Appl. Catal. B Environ.*, 2020, **269**, 118803.
75 H. Li, P. Wen, Q. Li, C. Dun, J. Xing, C. Lu, S. Adhikari, L. Jiang, D. L. Carroll and S. M. Geyer, *Adv. Energy Mater.*, 2017, **7**, 1700513.
76 W. Chen, Y. Zhang, G. Chen, R. Huang, Y. Zhou, Y. Wu, Y. Hu and K. Ostrikov, *J. Mater. Chem. A*, 2019, **7**, 3090–3100.

